ASME Journal of Turbomachinery
Online journal at:
https://asmedigitalcollection.asme.org/turbomachinery

Toward an In Situ Capable Method for Measuring Thermal Barrier Coating Thermal Resistance by Induction Phase Radiometry: Experimental Benchtop Demonstration

Shani Eitan
Turbomachinery and Heat Transfer Laboratory,
Faculty of Aerospace Engineering,
Technion—Israel Institute of Technology,
Haifa 3200003, Israel
e-mail: shanieitan@campus.technion.ac.il

Yaakov Gotman
Turbomachinery and Heat Transfer Laboratory,
Faculty of Aerospace Engineering,
Technion—Israel institute of Technology,
Haifa 3200003, Israel
e-mail: yaakovgotman@campus.technion.ac.il

Alexander Rakhman
Turbomachinery and Heat Transfer Laboratory,
Faculty of Aerospace Engineering,
Technion—Israel institute of Technology,
Haifa 3200003, Israel
e-mail: alexander.ra@technion.ac.il

Beni Cukurel[1]
Mem. ASME
Turbomachinery and Heat Transfer Laboratory,
Faculty of Aerospace Engineering,
Technion—Israel institute of Technology,
Haifa 3200003, Israel
e-mail: beni@cukurel.org

This study introduces an in situ approach to measuring the thermal resistance of thin ceramic coatings deposited on metallic substrates using induction phase radiometry. A one-dimensional analytical heat-transfer model is formulated that relates the phase lag between periodically modulated induction heating (with finite penetration depth) and the coating-surface temperature response as a function of coating thermal resistance. By periodically modulating the induction heating signal, a cyclic internal heat source is sustained within the substrate, and the phase lag between the electrical excitation and the coating-surface radiation flux is measured, enabling non-intrusive in situ evaluation without emissivity calibration or dedicated laboratory conditions. An experimental setup comprising an induction coil, function generator, pyrometer, and data-acquisition system is then designed and applied to an end-of-life gas turbine blade coated with a thermal barrier coating. Frequency-domain phase shifts measured over low modulation frequencies are fitted in a least-squares sense to the analytical model, and the coating thermal resistance is recovered from the best-fit parameters in an overdetermined system. The experimentally recovered thermal resistance shows a low overall residual error of 2% relative to the analytical model and with high repeatability, demonstrating robustness for potential field measurements and for future in situ, routine TBC health monitoring during gas turbine operational inspection without requiring engine removal. [DOI: 10.1115/1.4072552]

Keywords: thermal barrier coatings, unsteady heat transfer, induction heating, thermal resistance measurement technique, phase radiometry

Introduction

Thermal Barrier Coatings in Gas Turbine Environment. Gas turbines for propulsion and power generation operate at elevated temperatures well beyond the material limits, which allows them to achieve greater power density and efficiency. Along these lines, in addition to advancements in the material science of alloys, microstructure improvements of grain boundaries, and sophisticated cooling techniques, insulating ceramic layers are typically applied to the metal parts that are exposed to the highest temperatures (such as turbine vanes and blades, combustion chambers, and augmenters) [1].

Thermal barrier coating (TBC) is a multifunctional thin film characterized by its low thermal conductivity, high melting point, phase stability, exceptional fracture toughness, and relatively high thermal expansion coefficient. In gas turbine applications, TBCs are applied as a double-layered coating on the exposed surfaces of nickel- or cobalt-based superalloys, industrially deposited by either electron beam physical vapor deposition or plasma spraying [2].

A common TBC employed in modern gas turbine blades is yttria-stabilized zirconia (YSZ) with a thickness ranging from 100 μm to 2 mm, particularly in its metastable tetragonal-prime phase [3]. YSZ typically contains 7–8% Y_2O_3 by weight in ZrO_2, with diffusivity values reported between 3.6 and 5.6×10^{-7} m^2/s, and a thermal conductivity coefficient ranging from 0.42 to 0.98 W/m-K at room temperature [3,4]. Depending on deposition route, porosity, and thermal aging/sintering, reported YSZ conductivity can increase substantially (around 2.6 W/m-K); therefore, higher effective values are often used when modeling service-exposed coatings [5].

[1]Corresponding author.
Contributed by the International Gas Turbine Institute (IGTI) of ASME for publication in the Journal of Turbomachinery. Manuscript received May 15, 2026; final manuscript received June 23, 2026; published online August 25, 2026. Tech. Editor: David G. Bogard.

In the typical operational environment, several factors contribute to the degradation and reduced service life of TBCs. The YSZ coatings are prone to phase transitions at around 1470 K, where the metastable tetragonal-prime (t') phase shifts to a tetragonal (t) phase and eventually transforms into cubic and monoclinic phases during cooling [6]. This change in crystalline structure significantly enhances the sintering of YSZ, leading to decreased fracture toughness. Moreover, environmental dust plays a significant role in the degradation of the protective layer. This is in part due to abrasion, which reduces the layer thickness [7], but even in the absence of physical thinning, the thermal properties can deteriorate due to infiltration of Calcium–Magnesium–Alumina–Silicate, which can significantly increase thermal conductivity and diffusivity, negating the utility of the coating [8]. Given these challenges, routine inspection of TBCs is essential to ensure their continued functionality and to prevent airborne system availability issues caused by high rates of unscheduled engine removals.

Existing Approaches to Measuring Thermal Properties of Thin Films. The ability to assess thermal properties of TBCs is crucial for fleet operators, and the measurements should ideally be conducted in situ in order to provide a snapshot of thermal performance and predict life. Existing approaches can be divided into three categories depending on the excitation source and its time-dependent behavior.

The steady-state approach, exemplified by thin film thermal conduction [9], employs a constant heat flux source on a thin layer between two surfaces—often a substrate and a probe where temperature sensors on both sides quantify the gradient across and therefore the conductivity. However, the intrusive nature of the measurements on both sides renders it unsuitable for evaluation of installed parts.

As an alternative, the step change boundary condition methods (such as Laser Flash technique [4] and Pulsed Thermal Imaging Multilayer Analysis [10]) rely on analyzing the thermal response to transient heat sources; however, their accuracy depends on imposing well-defined boundary conditions (often necessitating vacuum environments, radiation shields, and high-emissivity coatings on specimens), which negates their ability to be used in situ.

Toward addressing the issue of emissivity correction, periodic excitation boundary condition methods (such as 3-Omega [4] and PopTea [11]) utilize modulated heat sources to analyze time-variant thermal responses, and the phase information processed through various analytical models provides the thermal resistance (R) of the thin layer, which can be expressed as a function of thermal diffusivity (α) and thickness (L):

$$R = L^2/\alpha \tag{1}$$

However, neither PopTea nor 3-Omega methods are suitable for in situ turbine blade measurements. The 3-Omega technique requires a deposited metal strip, incompatible with complex blade geometries, while PopTea depends on uniform surface absorption and bulky optical setups under controlled conditions; therefore, they are impractical for direct use within an assembled engine.

Motivation. TBCs are designed to provide long-term thermal protection for engine components, yet their performance degrades over time due to thermal cycling, erosion, and infiltration effects. There is a critical need for a reliable, noninvasive, and quantitative method to assess the thermal resistance of coatings directly on the component during its life. As a response to existing techniques that lack in situ applicability, this work experimentally demonstrates a calibration-free and direct measurement approach based on induction phase radiometry.

The proposed methodology measures the thermal resistance of TBCs by analyzing the phase lag between induced internal heating and the resulting thermal response at the surface. A low-frequency amplitude-modulated induction process generates periodic heating near the inner boundary of the ceramic layer and the metallic substrate interface. Specifically, a high-frequency carrier signal (~50 kHz) is modulated by a low-frequency signal (0.05–0.2 Hz) to create controlled, periodic internal heating within the alloy beneath the coating, which in turn creates a cyclic thermal response at the coating surface (via conduction), which can then be measured.

The experimental setup consists of a function generator that produces the modulated electrical signal, which is amplified and supplied to the induction coil positioned near the component to induce internal heating. The surface thermal response is then captured by a pyrometer, operating at a measurement frequency in the kHz range. The voltage input to the coil and the output signal from the pyrometer, which is proportional to the emitted radiation flux from the surface, are recorded simultaneously using a data-acquisition system across a range of modulation sweep frequencies. The key parameter extracted is the phase difference (in the frequency domain) between the low-frequency modulation signal applied to the coil and the thermal radiation response from the coating surface. The thermal resistance of the coating is calculated by minimizing the deviation between the experimentally measured phase data and predictions from an analytical conduction model in the least-square manner.

As the method relies solely on phase information, it does not depend on the absolute magnitude of the temperature response, eliminating the need for emissivity calibration. Additionally, as the heat is generated internally near the coating–substrate interface, rather than requiring external energy transmission through the ceramic layer, measurement accuracy is improved. Moreover, considering that the measurements are not highly sensitive to imposed boundary conditions, there is no need to create a controlled environment around the sample, offering a pathway for potentially in situ measurements.

Our previous work introduced the analytical model and the theoretical framework to recover thermal resistance from phase lag measurements of induction phase radiometry under varying considerations of noise and uncertainty [12]. Building upon this framework capturing the physics of heat conduction in the multi-layered slab together with the internal heat generation by the electromagnetic field, the current paper represents a natural progression by translating the model into experimental realization while addressing additional issues encountered. A test rig is designed and built, incorporating an induction heating circuit, a pyrometer, and a synchronized data-acquisition system to perform controlled modulation-frequency sweeps of induction heating on an actual coated turbine blade. This experimental validation demonstrates strong agreement with analytical predictions and confirms the robustness and operational feasibility to possibly employ induction phase radiometry as a noninvasive, in situ technique for assessing thermal barrier coating resistance on gas turbine components without significant sensitivity to boundary conditions or need for controlled environments. Although the method is demonstrated in a controlled bench-scale configuration, the term "in situ-capable" is used to denote the intended deployment pathway (inspection of installed components through constrained access), rather than a claim of full on-engine demonstration in the present study.

Methodology

Analytical Model. As detailed in Ref. [12], the analytical development of the measurement technique is based on a simplified two-layer heat conduction model consisting of a metallic substrate and a ceramic thermal barrier coating, subjected to periodic internal heat generation induced by modulated high-frequency induction heating. The formulation assumes one-dimensional heat conduction normal to the surface, with negligible contributions from the thin bond coat and no internal generation within the TBC itself.

In this context, negligible bondcoat contribution means the bond coat is not modeled as a separate inversion layer, not that its resistance is exactly zero. Its influence is lumped into the substrate-side phase term. This simplification is justified for thin metallic bond coats, whose characteristic thermal resistance L_{BC}/k_{BC} and diffusion timescale L_{BC}^2/α_{BC} are typically smaller than those of the ceramic topcoat in the modulation range considered here. Moreover, the 1D formulation is intended as a local approximation rather than a global airfoil model. The assumption is applied to measurement regions that are locally quasi-planar and located away from strong geometric discontinuities (e.g., film-cooling holes, edges, and abrupt curvature changes). Outside these conditions, lateral heat spreading can become non-negligible, and a higher-dimensional treatment is required.

The model further assumes a quasi-steady response to the high-frequency carrier signal, due to the large timescale separation of $O(10^5–10^6)$ between the high-frequency carrier and low-frequency modulation signals, and it treats internal generation as steady with varying amplitude.

Then, by solving the heat conduction equations in the frequency domain (applying a Laplace transform), with a nonhomogeneous boundary condition on the backside, representing the oscillating Joule heating, and a Robin condition at the surface, the relationship between the phase lag of the surface temperature response and the modulation frequency is derived [12]:

$$\phi_{TBC} = \tan^{-1}\left[\frac{\frac{\mathrm{Bi}}{2\mathrm{Wo}}\left[\begin{array}{c}\text{-}\sin(\mathrm{Wo})+\\ \cos(\mathrm{Wo})\tanh(\mathrm{Wo})\end{array}\right]\text{-}\sin(\mathrm{Wo})\tanh(\mathrm{Wo})}{\frac{\mathrm{Bi}}{2\mathrm{Wo}}\left[\begin{array}{c}\sin(\mathrm{Wo})+\\ \cos(\mathrm{Wo})\tanh(\mathrm{Wo})\end{array}\right]+\cos(\mathrm{Wo})}\right] + \phi_{\Delta} \tag{2}$$

where,

$$\phi_{\Delta} = \pi \cdot \min\left\{\frac{\mathrm{Re}(H(i\omega))}{|\mathrm{Re}(H(i\omega))|}, 0\right\} \tag{3}$$

and,

$$H(i\omega) = \frac{1}{\cos((1-i)\mathrm{Wo}) + \frac{(1+i)}{2}\frac{\mathrm{Bi}}{\mathrm{Wo}}\sin((1-i)\mathrm{Wo})} \tag{4}$$

where $H(i\omega)$ is the transfer function created by the ratio between the input backside thermal forcing and the output temperature over the surface.

The Womersley number, $\mathrm{Wo} = \sqrt{\omega L^2/2\alpha} = \sqrt{\omega \mathrm{R}/2}$, refers to a non-dimensional parameter that represents the ratio between pulsatile thermal forcing and the opposing effect of heat diffusion. For a surface natural convection heat-transfer coefficient of $h \sim O(5\ \mathrm{W/m^2\text{-}K})$, and TBC thickness, thermal conductivity, and diffusivity of $L \sim O(10^{-4}\ \mathrm{m})$, $k \sim O(5 \cdot 10^{-1}\ \mathrm{W/m\text{-}K})$, $\alpha \sim O(5 \cdot 10^{-7} \mathrm{m^2/s})$, and for a modulation frequency of $\omega \sim (10^{-2}\,\mathrm{Hz})$, the TBC thermal resistance is in the order of $R \sim O(5 \cdot 10^{-2})(s)$. Then, the Biot ($\mathrm{Bi} = hL/k$) and Womersley numbers can be estimated as $\mathrm{Bi} \sim O(10^{-3})$, $\mathrm{Wo} \sim O(10^{-2})$, resulting in the following ratio $\mathrm{Bi}/(2\mathrm{Wo}) \sim O(5 \cdot 10^{-2})$.

At the limit $\mathrm{Bi}/2\mathrm{Wo} \ll 1$, the 1-D phase expression can be represented as a direct function of the imposed modulation frequency, resulting in a closed-form solution:

$$\phi_{TBC} \approx \tan^{-1}[-\tan(\mathrm{Wo})\tanh(\mathrm{Wo})] \tag{5}$$

This consideration holds true for the typical properties and frequency range considered. It serves as the basis for recovering the coating's thermal resistance from measured phase lag data, as charted in Fig. 1 for the relevant range.

Now let us consider a typical TBC, with a thickness L_0, and thermal diffusivity α_0, yielding an unknown thermal resistance R_0. The value can be retrieved by controlling the induction coil to conduct a modulation frequency sweep, while measuring the surface radiation flux response at each frequency, and post-processing it to obtain phase-omega pairs that best fit the independent axis of resistance on the surface.

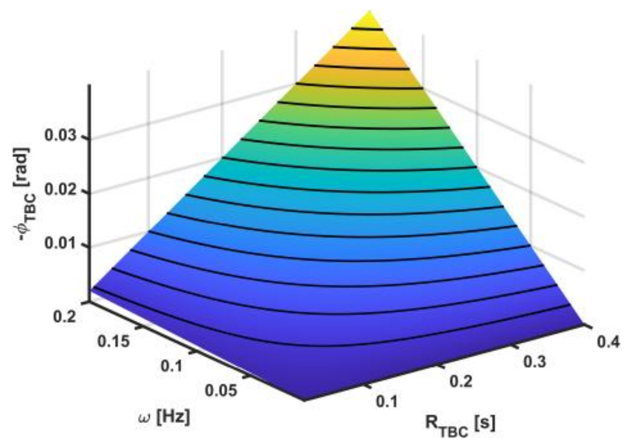

Fig. 1 Relationship of TBC surface phase angle ϕ with respect to modulation frequency ω and thermal resistance R

However, the measured phase is a linear superposition of heat conduction across both the TBC as well as the Inconel substrate, as the induction heating takes place at a finite penetration depth within the body. The Inconel phase delay ϕ_{INC}, is dependent on modulation frequency, metal's diffusivity, as well as the effective thickness representing the skin penetration depth, however, has negligible dependence on the thermal resistance of the TBC coating (R). Then, ϕ_{INC} can be directly solved using the 1one-layer heat conduction problem with heat generation:

$$\frac{1}{\alpha}\frac{\partial T}{\partial t} = \frac{\partial^2 T}{\partial^2 x} + \frac{g(x,t)}{k} \tag{6}$$

where $g(x,t)$ is the internal heat-generation distribution of the Joule heating, which was derived from Maxwell's equations for the modulated electrical field in the solid media case:

$$g(x,t) = \frac{\sigma^2 E_0^2 R_s}{4}\left[1 + \cos\left(2\omega_c t - \frac{2(x+d)}{\delta}\right)\right](1 + \cos(\omega_m t))\, e^{-\frac{2(x+d)}{\delta}} \tag{7}$$

where R_s is the effective substrate resistance, μ is the magnetic permeability, σ is the electrical conductivity, and ω_m is the modulation frequency. For a typical Inconel thermal conductivity value of $k = 12$ W/m-K, and a range of thickness and diffusivities (representing Inconel thermal resistance factor R_{INC}), the solution of ϕ_{INC} can be charted as a function of Womersley for the Inconel (Fig. 2). To highlight the differences in the phase relationship across the TBC, ϕ_{TBC}, Eq. (2) is also charted, highlighting the differences in local slope values. While both charts stem from the same basic heat-transfer equation, different source terms and boundary conditions ultimately affected their rate values. Inconel phase model included internal generation, whereas in the TBC phase problem formulation, a periodic surface temperature function was used at the interface. Regardless, for the same excitation frequency, the effective Womersley number for ϕ_{TBC} and ϕ_{INC} would not be the same, considering the differences in properties.

In the following, the total surface phase lag can be estimated as a linear summation of the Inconel and TBC diffusion delays ($\phi_{surface} = \phi_{INC} + \phi_{TBC}$) for any given combination of $\mathrm{W_o}$ for TBC and Inconel substrate (see Fig. 3).

Our prior work had assumed that ϕ_{INC} value can be estimated from the geometry and blade material properties (see Appendix

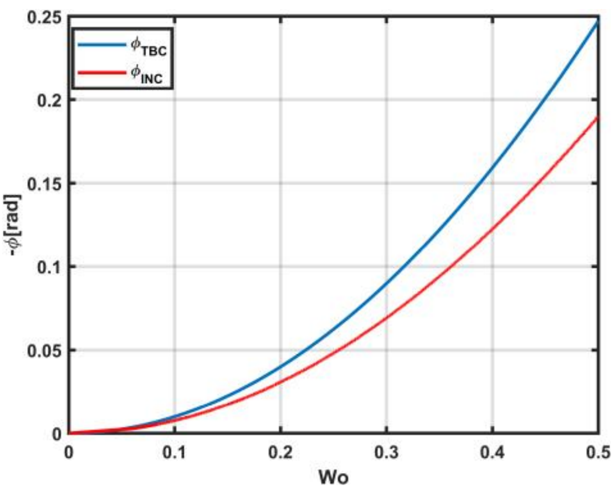

Fig. 2 Decoupled phase solution across TBC and Inconel substrate as a function of Womersley

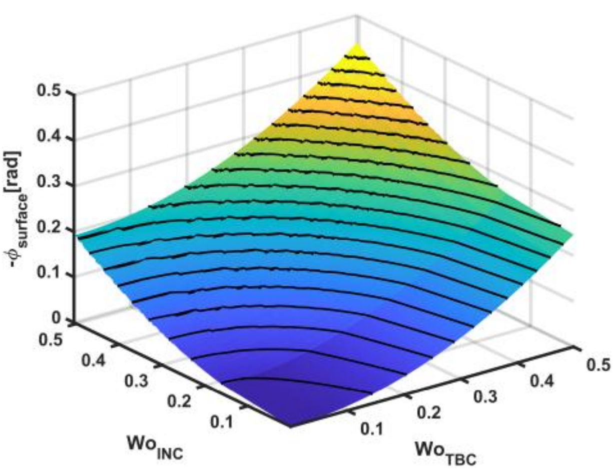

Fig. 3 Analytical solution of the phase at the surface (sum of Inconel and TBC diffusion phase delays), with respect to Womersley number

A for numerical simulations depicting Inconel substrate phase lag) and reached asymptotic constants for the large and small thickness limits [12]. In typical complex geometries, it is challenging to approximate the thermal diffusion by 1-D solutions, and it is worth defining an effective Inconel penetration depth or thickness L_{INC}. In this work, we extend the analytical solution framework to leave the effective thickness L_{INC} as a free variable. Then, an error function $\Delta\phi(\vec{\omega}, R_{INC}, R_{TBC})$ can be defined to quantify the difference between the experiments, and the model phase expressions (where R_{INC} contains the dependency to the variable L_{INC}). The resulting function can be wrapped in the interval $[-\pi,\pi]$:

$$\Delta\phi(\vec{\omega}, R_{TBC}, R_{INC}) = \pi - \\ ||\phi(\vec{\omega}) - \phi_{TBC}(\vec{\omega}, R_{TBC}) - \phi_{in}(\vec{\omega}, R_{INC})| - \pi| \tag{8}$$

Then, the absolute average error across all frequencies $\overline{|\Delta\phi(R_{TBC}, R_{INC})|}$ can be solved to obtain a minimum value in a least-squares sense, enabling the retrieval of R_{TBC}, R_{INC} pairs. Expanding these measurements for a set of repeated experiments across a range of frequencies will yield bounds of precision error.

Experimental Setup. The experimental setup consisted of a power supply, frequency-modulating function generator, and an induction coil as an electromagnetic field source connected to an amplifier circuit tailored for induction heating. Providing a voltage amplitude of 25 V with a 10 V offset at high power (up to 2000 W), the chosen induction board (Zero-Voltage Switching circuit by Aideepen) can work continuously, withstanding currents of up to 50 A, with sufficient heat dissipation due to large cooling fins and a fan interface (Fig. 4). The carrier frequency applied was 56 kHz, and amplitude modulation was conducted at multiple discrete frequencies.

The pyrometer used in this study ("Optris" OPTCTL3MLCF1) operates in a short-wave IR band (nominally around 2.3 μm) and was selected primarily due to its fast temporal response, which is essential for phase-resolved measurements under periodic modulation. Given the known wavelength-dependent semitransparency behavior of YSZ coatings, the measured signal in this band is interpreted as an effective radiometric response of the coating/substrate system rather than a strictly outer-surface-only radiance [5,13–16].

Radiative transfer through a semi-transparent TBC can introduce an additional phase component in the pyrometer signal, such that the measured phase is treated as a mixed quantity rather than purely conductive surface phase. To account for possible short-wave radiometric depth-mixing, the measured phase can be represented as:

$$\phi_{\mathrm{meas}}(\omega) = \phi_{\mathrm{cond}}(\omega; R_{TBC}, R_{INC}) + \phi_{\mathrm{opt}}(\omega) \tag{9}$$

where ϕ_{cond} is the conductive phase response and ϕ_{opt} is an optical-bias term associated with semitransparency-driven mixed emission [5,13,16]. In this work, ϕ_{opt} is not inverted as a full radiative-transfer field; instead, its impact is bounded using first-order sensitivity analysis (Appendix B). Therefore, recovered R_{TBC} and R_{INC} are interpreted as effective parameters for the present sensing band. This keeps the inverse recovery formulation unchanged while explicitly acknowledging non-ideal optical transmissivity effects.

The pyrometer was fixed above the coil at a focus distance of 200 mm (the original focal point distance of 85 mm was extended using a lens to avoid electromagnetic interference), resulting in a spot size of 2 mm. A hollow copper tube of 10-mm diameter with a wall thickness of 1.8 mm was wound seven times around a mean diameter of 40 mm, creating a coil of height 50 mm. The

Fig. 4 Induction heating circuit and TBC coated turbine blade

resultant coil is placed over balsa wood with an aperture of 5 mm, providing radiation shielding from the surroundings. The induction coil was operated in a non-contact configuration and was not bonded to the specimen. A controlled liftoff (air gap) was maintained between the coil and the blade surface during heating. Therefore, no adhesive or bonding interface existed between the coil and the specimen; coupling was purely electromagnetic.

The setup also included current sensors (SSA-100 by Riedon, Alhambra, CA) for measuring the electrical input to the induction coil. An NI cDAQ-9184 chassis with voltage input modules (NI-9263 and NI-9222) was used to record the sensor data. For the acquisition process, a LabVIEW code was written enabling simultaneous logging of both input and output signals and automatically setting the different modulation frequencies. The block diagram of the experimental setup can be found in Fig. 5.

In order to ensure accuracy of the recovery, the analytical expression for the TBC phase (Eq. (2), and also visualized in Fig. 1) indicates the requirement to discern values in the 0.001 rad order; and for a signal with a modulation frequency of 0.10 Hz, this would be manifested as a lag of ∼1.5 ms in the time domain. Therefore, considering the Nyquist criteria, the sampling rate was set to 3.78 kHz. (Moreover, it is also important to ensure that the pyrometer exposure time is small enough to resolve these changes, in 300–1000 μs range.)

The experiments were conducted on an end-of-life high-pressure turbine blade made of Inconel with a TBC coating, typically found in common engines (see Fig. 4). According to the engine OEM, the blade originally had a TBC thickness of 100–250 μm, and thickness measurements carried out using an eddy current sensor (Multiscope FMP10-20 by Fischer, Sindelfingen, Germany) yielded a value of 150 μm. An exemplary time series of pyrometer digital level and coil-current sensor output are presented in Fig. 6 for a single modulation frequency value. Evidently, there is clearly a time lag in the periodic oscillations between the radiation flux as measured by the pyrometer and the electrical current supplied to the coils, which creates the varying electromagnetic field that forms periodic Joule heating inside the Inconel substrate.

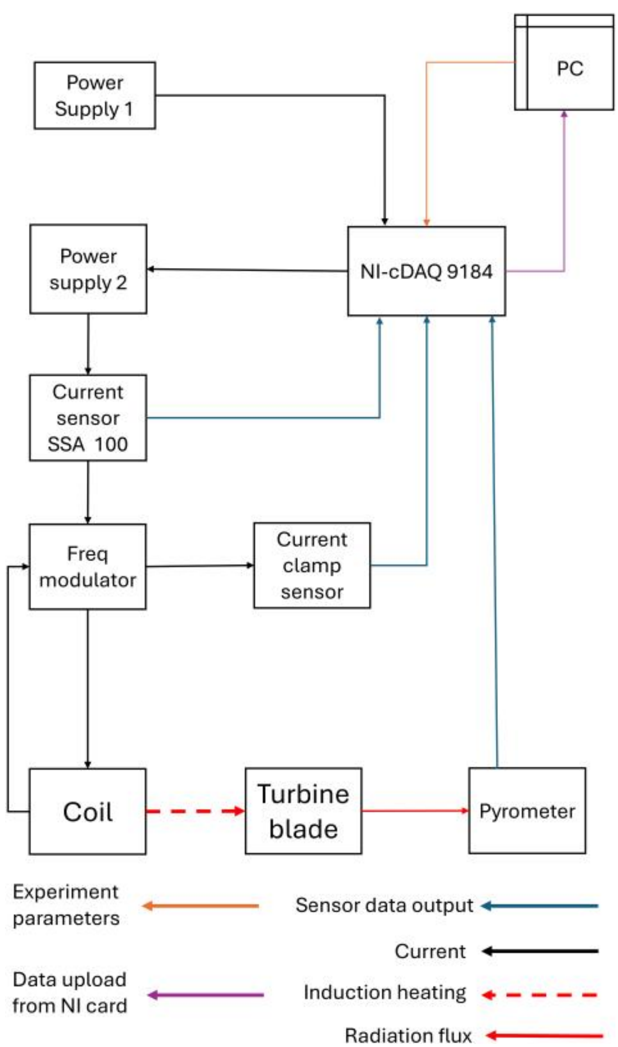

Fig. 5 Experimental setup block diagram for induction phase radiometry

Data Processing. Toward extracting the relative phase of the pyrometer digital level reading with respect to the current signal, the data series is transformed into the frequency domain. The conventional Fast Fourier Transform with a Hanning window (good spectral leakage reduction and frequency resolution properties) didn't result in sufficiently repeatable results, as a non-stationary drift in the signal was observed due to the change in amplifier circuit temperature due to insufficient electronics cooling.

Instead, Short-Time Fourier Transform (STFT) was conducted by sliding an analysis window of a predefined length over the signal and calculating the Discrete Fourier Transform for each data segment. The window translates over the original signal at predefined intervals, equivalent to the overlap between adjoining segments. Most window functions taper off at the edges to avoid spectral ringing. The resultant set of complex values of each windowed segment is added to a matrix that contains the magnitude and phase information for each time interval. Then, by selecting the phase of the frequency where the most significant amplitude peak appears in the power spectral density, the average phase of the modulation frequency can be computed across the data set (Fig. 7).

This average phase difference (between the current input and radiation flux output signals) was calculated for an increasing number of cycles until convergence was achieved. Figure 8 depicts an example of average phase convergence deviation for $f = 0.12$ Hz at increasing number of measurement cycles, $\frac{\phi_{n+1} - \phi_n}{\phi_n}\%$. The resultant phase convergence error was below $10^{-3}\%$ after 100 cycles. Therefore, we used an average of 200 cycles for each frequency. Comparing repeated measurements at the same frequency and number of cycles to their mean value

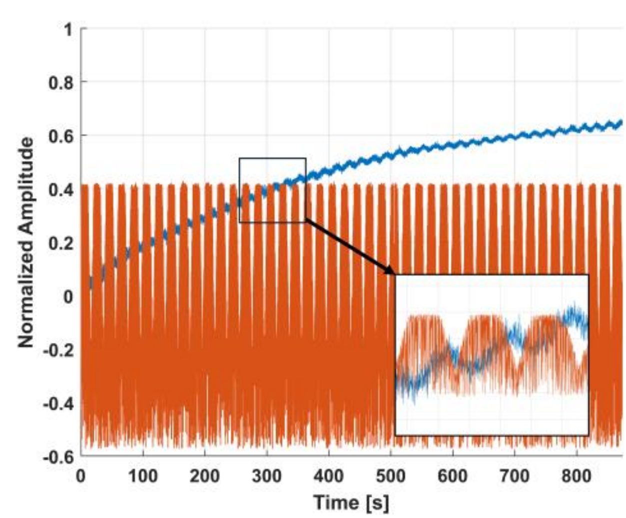

Fig. 6 Exemplary surface radiation flux and induction coil current signals at 0.08 Hz amplitude modulation

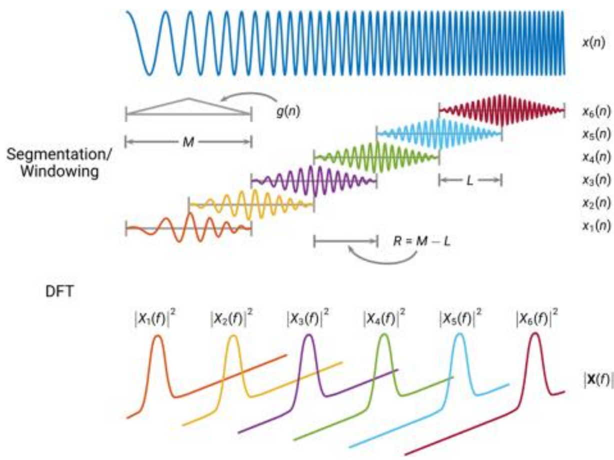

Fig. 7 Representation of the short-time Fourier transform

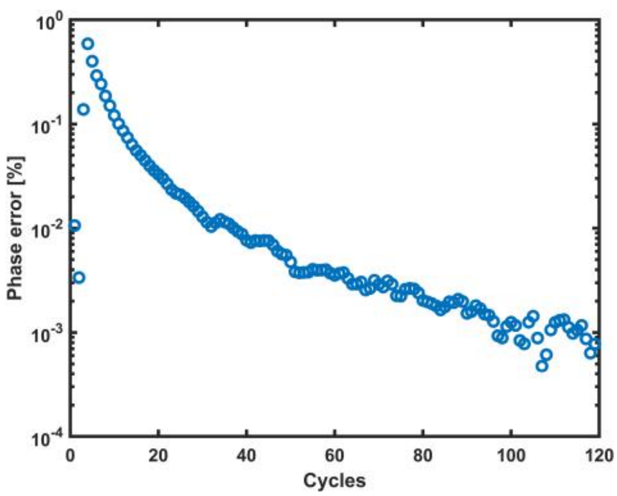

Fig. 8 Exemplary phase convergence error for increased number of cycles for a fixed modulation frequency

showed that the repeatability of the phase extraction for a single sample is in the order of 0.1%.

It is worthwhile to note that the pyrometer is used here as a radiometric detector of periodic signal content, not as an absolute thermometry device. Specifically, only the phase of the pyrometer signal at the modulation frequency is used in the inversion. An opaque surface with approximately time-invariant emissivity in the measurement band, $I(t) = \varepsilon_\lambda B_\lambda(T(t))$, and linearization around the operating point yields $\tilde{I}_\omega \propto \varepsilon_\lambda \tilde{T}_\omega$. Hence, emissivity scales signal magnitude but does not affect the extracted phase, so absolute emissivity calibration is not required for phase-only recovery under this approximation. When finite semitransparency and/or wavelength-dependent volumetric radiative contribution is present, an additional optical phase-bias term may arise; in this work, that contribution is treated as a bounded measurement uncertainty term in the phase budget.

Results

Varying the coil modulation frequency at nine discrete values ranging from 0.01 Hz to 0.20 Hz, induction heating supply current and pyrometer digital level readings were recorded and analyzed using STFT phase averaging for each considered frequency. The resultant data contains a set of phase values at differing modulation frequencies (Fig. 9). As the measurements are stemming from an unknown yet fixed thermal resistance value,

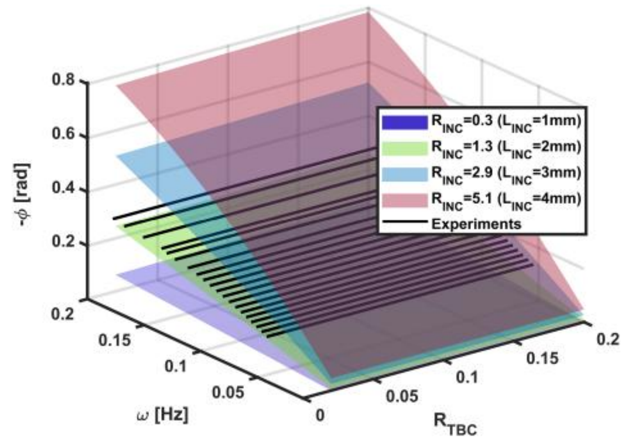

Fig. 9 Total phase lag measurements at differing modulation frequencies, and model predictions depending on TBC and Inconel thermal resistances

and do not vary with the free variable, they are indicated as horizontal lines along the R_{TBC} axis.

In order to better understand the dependencies of the problem, the analytical solution of the total phase delay $\phi_{surface}$ is also charted in Fig. 9 for different R_{TBC} and R_{INC}, evaluated at each frequency ω. In order to provide an order-of-magnitude sense of the effective thickness, R_{INC} is also converted to L_{INC}, assuming Inconel diffusivity of $3.1 \cdot 10^{-6}$ m^2/s. A wrapping of π was applied to the calculated values, and an additional constant bias shift was added to negate the gap between the model and experiments resulting from multi-dimensional effects, computed such that the difference at the "steady-state" condition (i.e., $\omega = 0$) matches the experimental values. Figure 9 clearly portrays that the experimental readings fall uniformly between the different computed surfaces derived from the model; it can be deduced that the tested sample has an effective Inconel penetration depth of L_{INC}, which lies between 2 and 3 mm, consistent with skin depth calculation for Inconel $\delta = \sqrt{2/\omega_c \mu \sigma}$ at 56 kHz, yielding ~2.4 mm [17].

Analyzing the findings in the non-dimensional parameter space, the total phase can be charted as a function of $\mathrm{Wo_{TBC}}$ and the ratio of TBC to Inconel thermal resistance combinations (for consistency represented as ratio of $\mathrm{Wo_{INC}}/W_{\mathrm{TBC}}$; Fig. 10). Then, the

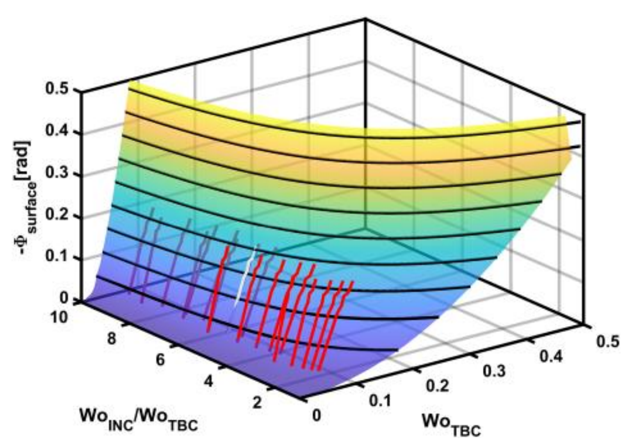

Fig. 10 Total phase lag measurements at differing modulation frequencies represented in non-dimensional space as a function of $\mathbf{Wo_{INC}}$ and $\mathbf{Wo_{TBC}}$, where the lines indicate experimental data as represented by differing potential combinations of $\boldsymbol{R_{TBC}}$ and $\boldsymbol{R_{INC}}$ (indicated by the ratio of $\mathbf{Wo_{INC}/Wo_{TBC}}$)and model predictions form a surface

experimental data spans a set of lines in 3D space with differing multipliers (in reality, the resolution of the optimization is much higher than indicated in the chart), and the R_{TBC} and R_{INC} combinations from the model form a surface. Then, the line which falls onto the surface in the least-square sense represents the best-fit solution pair. While some of the curves are clearly above or below the surface, there are lines that are as close to the surface, following its topology, as required for the fitting process precision. Figure 11 portrays the local phase error between the hypothetical thermal resistance combinations as represented by the lines and the model surface. Differing lines can also be interpreted as changing Wo_{INC}/W_{TBC} ratios (if one was to be kept constant, considering the parametric variations of R_{TBC} and R_{INC} can result in non-unique ratios). Clearly, there is a particular line combination, which provides minimum local error (across the entire data range (indicated in a different line color in Figs. 10 and 11). In order to highlight this observation, for the same thermal resistance combinations, Fig. 12 considers the RMS phase error across the entire Wo_{TBC} range for each line (average of Fig. 11), and it can be seen that there is a uniform convergence toward a specific value, Wo_{INC}/Wo_{TBC} combination of 5.168. In the following, knowing the measurement frequencies, the R_{TBC} can be recovered from the best-fit curve, resulting in $R_{TBC} = 0.101$ s.

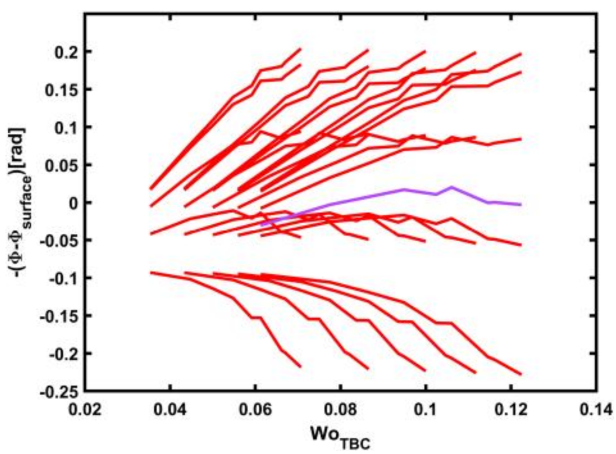

Fig. 11 Total phase deviations between measurements and model predictions for differing potential combinations of R_{TBC} and R_{INC}, indicated by different lines across Wo_{TBC} space

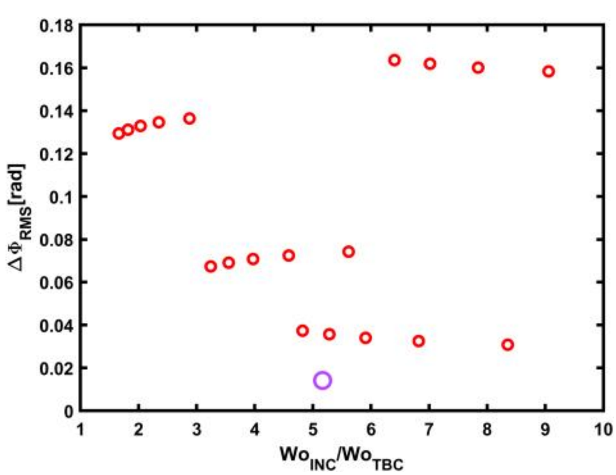

Fig. 12 Average error in phase between measurements and model predictions for differing potential combinations of R_{TBC} and R_{INC}

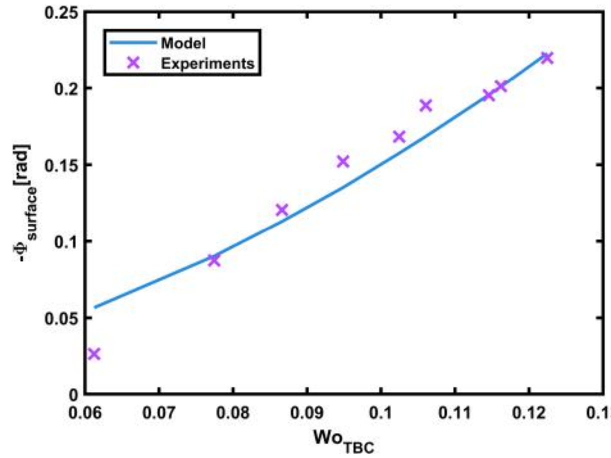

Fig. 13 Phase model for the optimal of Wo_{INC}/W_{TBC} ratio and experimental results indicating the goodness of the overdetermined fit

Table 1 Phase data comparison between measurements and model

Measurements		Model			
$\omega(Hz)$	$-\phi(rad)$	Wo_{TBC}	Wo_{INC}	$-\phi_{TBC}$(rad)	$-\phi_{INC}$(rad)
0.050	0.0265	0.0512	0.2648	0.0026	0.0540
0.080	0.0874	0.0648	0.3349	0.0042	0.0861
0.100	0.1205	0.0725	0.3744	0.0052	0.1077
0.120	0.1521	0.0794	0.4102	0.0063	0.1288
0.140	0.1683	0.0857	0.4430	0.0073	0.1502
0.150	0.1887	0.0887	0.4586	0.0079	0.1606
0.175	0.1952	0.0959	0.4953	0.0092	0.1863
0.180	0.2013	0.0972	0.5023	0.0094	0.1915
0.200	0.2199	0.1025	0.5295	0.0105	0.2122

The same optimal Wo_{INC}/Wo_{TBC} combination is charted from the model in Fig. 13 with respect to total phase measurements (data provided in Table 1) and non-dimensionalized in the same form. The accuracy of the physical model is indicated by the close match between the symbols indicating the measurements and the line representing the model. The goodness of the overdetermined fit is 0.014 rad in a root-mean-squared sense (as seen in Fig. 12).

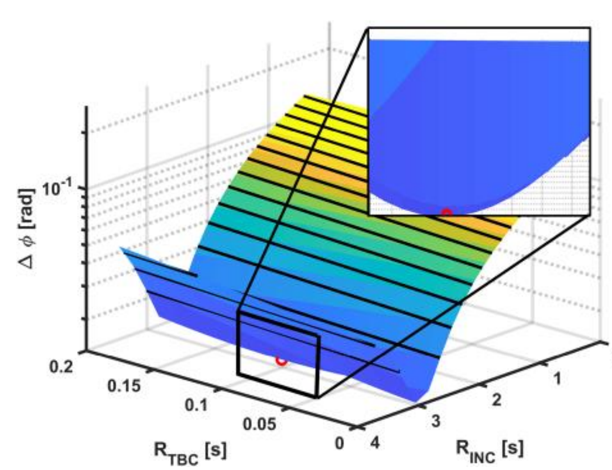

Fig. 14 Total modulation-frequency-averaged phase error function between the experiments and the model as a function of R_{TBC} and R_{INC}

This fitting process can also be directly represented by the error function in Eq. (8), averaged over the modulation frequencies considered (Fig. 14). It is seen that the same minimum can be retrieved while incorporating the parametric thermal resistance representation of both layers. The residual average phase error is 0.28 rad (i.e., ~2% error with respect to the measured value). Applying the definition of thermal resistance for the recovered value of R_{TBC}, thickness and thermal diffusivity coefficient can be mapped out (Fig. 15). For the measured TBC thickness of 150 μm, the corresponding thermal diffusivity is 2.5 10^{-7} $\mathrm{m^2/s}$, typical for a heavily used YSZ coating [14,18].

Sensitivity of Thermal Resistance to Phase Error

Having demonstrated the concept of thermal resistance recovery, the uncertainty due to error propagation in phase reading and current modulation frequency is analyzed. Considering the relationship between the phase difference and the Womersley number (as given in Eq. (5)), for typical Wo numbers in the 0.1–0.2 range, its dependency can be further simplified considering $\tan(\epsilon) \cong \tanh(\epsilon) \cong \epsilon$, resulting in the following expression,

$$\phi_{\mathrm{TBC}} \cong \frac{\omega}{2} R_{TBC} \tag{10}$$

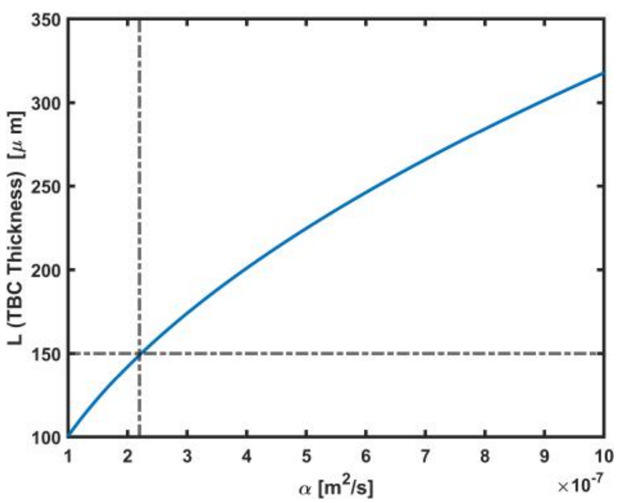

Fig. 15 TBC Thickness and thermal diffusivity coefficient relation for the recovered $R = 0.101$ s

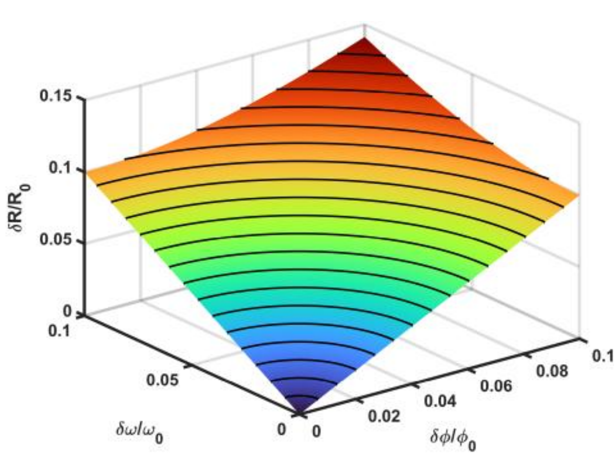

Fig. 16 Thermal resistance error due to uncertainty in modulation frequency and phase delay

which can then be used to define the thermal resistance uncertainty,

$$(\delta R_{\mathrm{TBC}})/2 = \sqrt{(\omega^{-1}\delta\phi_{TBC})^2 + (\phi_{TBC}\omega^{-2}\,\delta\omega)^2} \tag{11}$$

Evaluated for nominal values of $\omega_o = 0.1\,\mathrm{Hz}$, $R_o = 0.1$, and $\phi_o = 0.005\,\mathrm{rad}$, the percent thermal resistance error $\delta R/R_o$ is charted in Fig. 16 for varying levels of error in modulation frequency $\delta\omega/\omega_o$, and diffusion phase delay $\delta\phi/\phi_o$. It can be seen that there exists a nearly linear dependency to frequency and phase noise. However, when both errors are combined, the total uncertainty can grow (e.g., 10% bias in frequency together with 10% bias in phase would create almost 15% uncertainty in the recovery). Thus, in prospective engine implementations, both sources of uncertainty must be tightly controlled by careful design of the excitation and acquisition chain (circuit layout and cooling, data-acquisition hardware, pyrometer characteristics, function generator stability, etc.) to ensure accurate TBC resistance retrieval.

Summary and Conclusions

This work experimentally demonstrates an in situ method for determining the thermal resistance of thermal barrier coatings based on the phase lag between periodically modulated induction heating of Inconel and the resulting surface radiation from the surface of the airfoil after conduction. Building on earlier studies that validated the analytical model and recovery algorithm using only synthetic data, the present study implements the technique on a dedicated experimental rig and applies it to real measurements from a blade specimen.

The induction coil–pyrometer setup, operated over a range of modulation frequencies, produced repeatable radiation time series that were processed to extract the fundamental phase. After mitigating electromagnetic interference through increased standoff distance, line-of-sight shielding, and controlled specimen alignment, the measured phase converged to a stable value of ~1.6 rad, with repeatability better than 0.1%. Sensitivity analysis showed an essentially linear dependence of the recovered thermal resistance on uncertainties in both modulation frequency and phase, emphasizing the importance of coil-current excitation frequency and phase-extraction accuracy.

Application of the phase-minimization recovery procedure yielded a single well-defined minimum in the R_{TBC}–R_{INC} space. The corresponding TBC thermal properties fall within the expected range for service-exposed YSZ coatings. The recovered thermal resistance exhibited a deviation from the analytical model below 2%, indicating that the method can retrieve TBC thermal resistance with relatively low uncertainty under experimental conditions.

The present inversion is therefore interpreted as effective in situ parameter recovery under short-wave sensing, where semi-transparency-driven radiometric mixing can introduce additional phase bias. Despite the uncertainty band, the primary trends remain robust. For nominal absolute-property extraction with tighter uncertainty margins, long-wave sensing and/or explicit thermo-radiative forward modeling is recommended.

The present implementation remains subject to practical constraints such as coil positioning and line-of-sight access for the pyrometer. Within these limits, however, the results provide, to the authors' knowledge, the first experimental validation of induction phase radiometry as a viable route to in situ TBC thermal resistance measurement on turbine components. Future work will focus on benchmark specimens with independently characterized properties to refine the uncertainty budget, mapping spatial variations along actual blade geometries, and developing miniaturized, integrated coil–pyrometer assemblies suitable for insertion into engine hardware through the borescope hole, ultimately enabling on-wing health monitoring of thermal barrier coatings.

Funding Data

- European Research Council (ERC) (Grant No. 853096; Funder ID: 10.13039/501100000781).
- Minerva Foundation (Grant No. AZ5746940764; Funder ID: 10.13039/501100001658)

Conflict of Interest

There are no conflicts of interest.

Data Availability Statement

The datasets generated and supporting the findings of this article are obtainable from the corresponding author upon reasonable request.

Nomenclature

c = carrier (high-frequency induction signal)
f = low-frequency modulation frequency
h = natural convection heat-transfer coefficient at outer surface
k = thermal conductivity
t = time
x = spatial coordinate normal to the surface
E = electrical field
H = transfer function between imposed thermal forcing and surface temperature response
I = induction-coil current
L = coating thickness (TBC layer)
N = number of modulation-frequency samples used in the fit
R = thermal resistance (defined in this work as $R = L^2/\alpha$)
T = temperature
U = electrical voltage (excitation)
V = voltage (generic)
f_c = high-frequency carrier (induction) frequency
I_{meas} = measure radiance
L_{eff} = effective substrate thickness/effective penetration depth used in 1-D model fitting
R_{BC} = bondcoat thermal resistance
R_s = electrical resistance
R_{TBC} = thermal resistance of the TBC layer
R_{INC} = effective thermal resistance parameter of the substrate layer
$g(x,t)$ = volumetric internal heat-generation rate
Bi = Biot number; compares surface convection to internal conduction (TBC layer)
LI = radiance
Wo = Womersley number; compares oscillatory thermal forcing timescale to diffusion timescale
Wo_{TBC} = Womersley number based on TBC properties
Wo_{INC} = Womersley number based on substrate effective properties
α = thermal diffusivity
α_0 = nominal/reference thermal diffusivity
δ = electromagnetic skin depth (penetration depth) in substrate
ε = emissivity
μ = magnetic permeability
ρ = density
σ = electrical conductivity
τ_{BC} = bondcoat diffusion timescale
φ = phase lag between electrical excitation (or coil-current modulation) and surface thermal response
$\Delta\varphi$ = error of phase lag
$\phi_{meas}(f)$ = measured phase
ϕ_{cond} = conductive term phase
$\phi_{opt}(f)$ = semitransparency-driven bias
ω = angular frequency ($\omega = 2\pi f$)
wi_{sub} = substrate radiance fraction

Abbreviations

0 = nominal/reference value
APS = atmospheric plasma spraying
CMAS = Calcium–Magnesium–Alumina–Silicate
COMSOL = COMSOL Multiphysics®
DAQ = data acquisition
DFT = Discrete Fourier Transform
eff = effective value used for reduced 1D representation/fitted parameter
FFT = Fast Fourier Transform
INC = substrate (Inconel/superalloy) layer
IR = infrared
NI = National Instruments
OEM = original equipment manufacturer
PopTea = periodic optical (thermal) excitation technique (as cited in the paper)
STFT = Short-Time Fourier Transform
TBC = thermal barrier coating layer
YSZ = Yttria-stabilized zirconia
ZVS = zero-voltage switching

Appendix A: Numerical Simulation of Induction Heating

In addition to the analytical model, a numerical simulation framework was constructed to evaluate heat-transfer behavior under periodic Joule heating and to provide additional context for the analytical and experimental results. The primary objectives were to compute the temperature response and phase behavior over a range of modulation frequencies. A transient simulation of the unsteady heating was performed using the COMSOL Induction Heating Module. The model was designed to replicate the actual coil geometry as closely as possible and included an electromagnetic insulator aperture to confine the radiation flux to the center of the coil footprint on the blade surface.

A 2D axisymmetric model in (r, z) coordinates was adopted. The specimen was represented as a cross section of a two-layer body with an outer radius of 150 mm. The first layer comprised the metallic substrate (blade) with a thickness of 5 mm, and the upper 150-μm thick layer formed the TBC. The spring-shaped induction coil was represented as a series of circular rings formed from hollow circular cross sections. The key geometric parameters included the coil cross section (outer radius $R_{c,out} = 5$ mm, inner radius $R_{c,in} = 3.2$ mm), winding diameter (40 mm center-to-center), number of turns (7), and overall coil height (50 mm). Thermal boundary conditions consisted of an axisymmetric boundary on the left side, an adiabatic boundary on the right side, and a fixed temperature at the bottom of the Inconel substrate. Natural convection (with $h = 5$ W/m^{2}K) was applied to the outer TBC surface. The aperture block consisting of a centered viewing port (radius 5 mm) for surface radiation measurements was also modeled. The surrounding air domain was represented by a 200-mm radius sphere enclosing the specimen and coil to capture natural convection. The computational domain can be seen in Fig. 17.

The materials considered were Inconel X-750 for the blade substrate, YSZ for the TBC, copper for the coil, and Balsa wood as the aperture. The properties implemented in the model are summarized in Table 2, including thermal diffusivity, thermal conductivity, electrical conductivity, permeability, specific heat, electrical resistivity, and mass density. The thermal conductivity value is chosen to represent an aged/sintered effective coating state and lies within reported ranges for heat-treated EB-PVD YSZ [5].

The mesh contained ~20,000 triangular elements, with refinement near the coil, across the TBC thickness, and along the

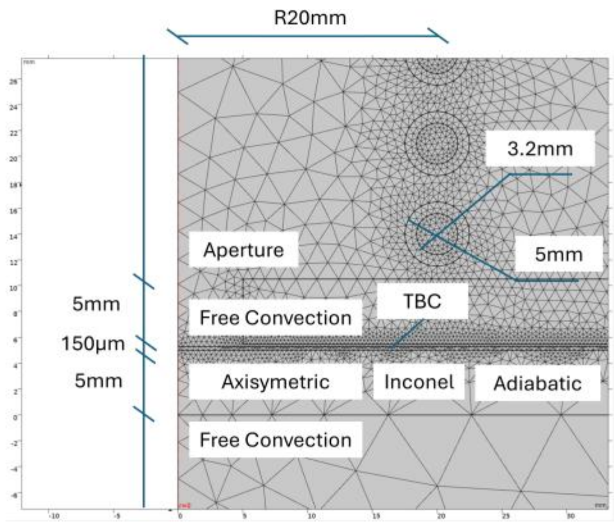

Fig. 17 Numerical simulation domain and boundary conditions

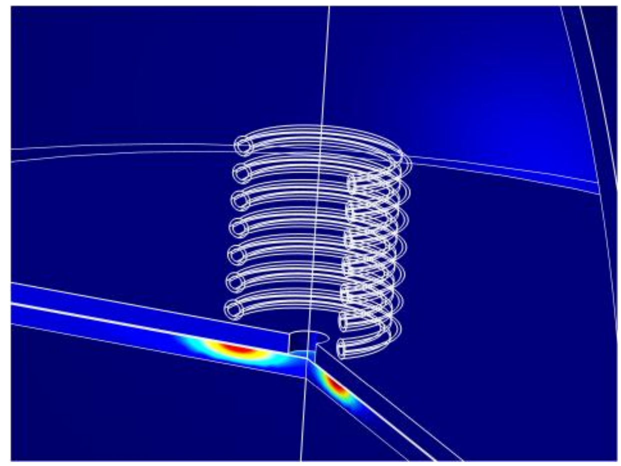

Fig. 18 Visualization of axisymmetric induction heating inside the Inconel workpiece

Table 2 Material properties implemented in COMSOL simulations

Property	Inconel	YSZ	Copper	Balsa
Thermal diffusivity (m^2/s)	$3.1 \cdot 10^{-6}$	$4 \cdot 10^{-7}$	—	$7.5 \cdot 10^{-7}$
Thermal conductivity (W/mK)	12	2	—	0.15
Electrical conductivity (S/m)	$8.2 \cdot 10^5$	0	$6 \cdot 10^{-7}$	0
Permeability	1.0035	1	1	1
Specific heat (J/kg K)	431	418	—	2000
Electrical resistivity (Ω m)	$1.22 \cdot 10^{-6}$	—	$1.7 \cdot 10^{-8}$	—
Density (kg/m^3)	8280	2000	8960	100

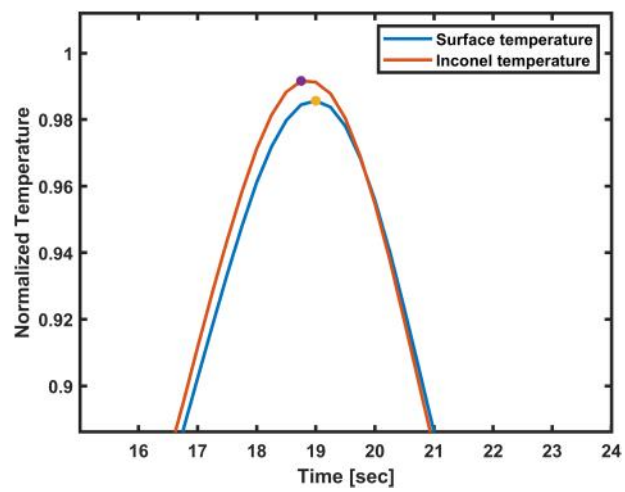

Fig. 19 Exemplary normalized temperature signal in the time domain for the Inconel interface and YSZ surface

TBC–air interface in the measurement region. The field-solution convergence tolerance was set to 0.01%. Time stepping was selected to resolve small phase differences in the low-frequency response; however, sufficiently small time-steps substantially increased runtime and limited the practicality of using the full transient numerical model for broad parametric sweeps. Consequently, the analytical expressions were used in the main recovery framework, while the numerical model served as a validation and design-support tool.

The spiral coil was driven with an amplitude-modulated sinusoidal current of sufficient magnitude to generate clear, periodic temperature oscillations. Figure 18 visualizes the axisymmetric induction heating inside the Inconel workpiece (coated specimen and induction coil) together with a representative temperature field, providing qualitative context for the simulated heat-flow path and the region of interest. For phase analysis, the simulated temperature time series were processed using the same phase-extraction procedure applied to the experimental signals. The resulting phase lag, and the corresponding phase difference between the substrate response and the coating-surface signal are illustrated in Fig. 19 using representative interface and surface temperature traces. Overall, the numerical model shows excellent agreement with both the experimentally measured phase response and the analytical formulation, with agreement within 0.1% for the coating-surface phase at the considered modulation frequencies of 0.07–0.08 Hz.

To quantify the validity range of the local 1D approximation, we conducted supporting COMSOL simulations including periodic induction heating and transient conduction in 2D. For radial nonuniformity within the coil opening, the phase deviation between the center point and an off-center location at $r/R_{co} = 0.05$ is on the order of ~ 0.05 rad, although amplitude varies spatially. This indicates that phase is comparatively robust in the central measurement region. Curvature sensitivity was also assessed using segments with radii $s = 29 - 135$ mm and $R_{co} = 24$ mm. Relative to the flat-reference case, curvature-induced phase bias remains around ~ 0.05 rad near $s/R_{co} \approx 6$, providing a practical geometric bound for reliable use of the simplified model.

Appendix B: First-Order Estimate of Substrate Radiative Contribution and Phase Bias

This appendix provides a bounded first-order estimate of short-wave optical mixing effects. Measured radiance is approximated as:

$$LI_{\text{meas}} \approx \varepsilon_c B(T_c) + \tau_c \varepsilon_s B(T_s) \quad (12)$$

with substrate radiance fraction:

$$wi_{\text{sub}} = \frac{\tau_c \varepsilon_s B(T_s)}{\varepsilon_c B(T_c) + \tau_c \varepsilon_s B(T_s)} \quad (13)$$

For near-isothermal comparison ($B(T_s) \approx B(T_c)$):

$$wi_{\text{sub}} \approx \frac{\tau_c \varepsilon_s}{\varepsilon_c + \tau_c \varepsilon_s} \quad (14)$$

Thermal phase separation across coating thickness is estimated by:

$$\Delta\phi_{th}(\omega) \approx L\sqrt{\frac{\pi\omega}{\alpha}} \quad (15)$$

The phase-bias magnitude from two-component mixing can be estimated by:

$$\delta\phi = \text{atan2}(wi_{\text{sub}} \sin \Delta\phi_{th}(1 - wi_{\text{sub}}) + wi_{\text{sub}} \cos \Delta\phi_{th}) \quad (16)$$

Baseline assumptions ($\varepsilon_c = 0.2$, $\tau_c = 0.8$, $\varepsilon_s = 0.6$) yield $wi_{\text{sub}} = 0.706$ and $\delta\phi = \{0.038, 0.084, 0.119\ 0.168\}$ rad, for $\omega = \{0.01, 0.05, 0.10, 0.20\}$Hz.

These values are intended as first-order sensitivity bounds (not full radiative-transfer inversion) and justify interpreting recovered parameters as effective values under the present short-wave sensing configuration.

References

[1] Parker, D. W., 1992, "Thermal Barrier Coatings for Gas Turbines, Automotive Engines and Diesel Equipment," Mater. Des., **13**(6), pp. 345–351.

[2] Thakare, J. G., Pandey, C., Mahapatra, M. M., and Mulik, R. S., 2021, "Thermal Barrier Coatings—A State of the Art Review," Met. Mater. Int., **27**(7), pp. 1947–1968.

[3] Clarke, D. R., Oechsner, M., and Padture, N. P., 2012, "Thermal-Barrier Coatings for More Efficient Gas-Turbine Engines," MRS Bull., **37**(10), pp. 891–898.

[4] Taylor, R. E., Wang, X., and Xu, X., 1999, "Thermophysical Properties of Thermal Barrier Coatings," Surf. Coat. Technol., **120–121**, pp. 89–95.

[5] Manara, J., Arduini-Schuster, M., Rätzer-Scheibe, H.-J., and Schulz, U., 2009, "Infrared-Optical Properties and Heat Transfer Coefficients of Semitransparent Thermal Barrier Coatings," Surf. Coat. Technol., **203**(8), pp. 1059–1068.

[6] Song, N., Wang, Z., Xing, Y., Zhang, M., Wu, P., Qian, F., Feng, J., Qi, L., Wan, C., and Pan, W., 2019, "Evaluation of Phase Transformation and Mechanical Properties of Metastable Yttria-Stabilized Zirconia by Nanoindentation," Materials, **12**(10), p. 1677.

[7] Swar, R., Hamed, A., Shin, D., Woggon, N., and Miller, R., 2012, "Deterioration of Thermal Barrier Coated Turbine Blades by Erosion," Int. J. Rotating Mach., **2012**(1), p. 601837.

[8] Kakuda, T. R., Levi, C. G., and Bennett, T. D., 2015, "The Thermal Behavior of CMAS-Infiltrated Thermal Barrier Coatings," Surf. Coat. Technol., **272**, pp. 350–356.

[9] Subramanian, C. S., Amer, T., UpChurch, B. T., Alderfer, D. W., Burkett, C., and Sealey, B., 2006, "New Device and Method for Measuring Thermal Conductivity of Thin-Films," ISA Trans., **45**(3), pp. 313–318.

[10] Sun, J. G., 2014, "Pulsed Thermal Imaging Measurement of Thermal Properties for Thermal Barrier Coatings Based on a Multilayer Heat Transfer Model," ASME J. Heat Transfer, **136**(8), p. 081601.

[11] Kakuda, T., Limarga, A., Vaidya, A., Kulkarni, A., and Bennett, T. D., 2010, "Non-Destructive Thermal Property Measurements of an APS TBC on an Intact Turbine Blade," Surf. Coat. Technol., **205**(2), pp. 446–451.

[12] Eitan, S., Julius, S., and Cukurel, B., 2024, "In-Situ Measurement of Thermal Barrier Coating Properties via Induction Phase Radiometry: Methodology Development," ASME J. Heat Mass Transfer, **146**(4), p. 043801.

[13] Eldridge, J. I., Spuckler, C. M., Street, K. W., and Markham, J. R., 2002, "Infrared Radiative Properties of Yttria-Stabilized Zirconia Thermal Barrier Coatings," Proceedings of the 26th Annual Conference on Composites, Advanced Ceramics, Materials, and Structures: B, Ceramic Engineering and Science, Cocoa Beach, FL, Jan. 13–18, Vol. 23, No. 4, pp. 417–430.

[14] González-Fernández, L., del Campo, L., Pérez-Sáez, R. B., and Tello, M. J., 2012, "Normal Spectral Emittance of Inconel 718 Aeronautical Alloy Coated With Yttria-Stabilized Zirconia Films," J. Alloys Compd., **513**, pp. 101–106.

[15] Manara, J., Brandt, R., Kuhn, J., Fricke, J., Krell, T., Schulz, U., Peters, M., and Kaysser, W. A., 2000, "Emittance of Y_2O_3-Stabilised ZrO_2 Thermal Barrier Coatings Prepared by Electron-Beam Physical-Vapour Deposition," High Temp.-High Press., **32**(3), pp. 361–368.

[16] Lim, G., and Kar, A., 2009, "Radiative Properties of Thermal Barrier Coatings at High Temperatures," J. Phys. D: Appl. Phys., **42**(15), p. 155412.

[17] Hayt, W. H., Jr., and Buck, J. A., 2012, *Engineering Electromagnetics*, 8th ed., McGraw-Hill, New York.

[18] Liu, T., Qiu, Y., Liu, Y., Liu, Z., Deng, Z., Guo, Z., Wang, F., et al., 2025, "Fabrication and Characterization of Multilayer YSZ Thermal Barrier Coating by Detonation Spraying and Atmospheric Plasma Spraying," Ceram. Int., **51**(20), pp. 30525–30536.